Detecting the earliest stages of giant planet formation in scattered light

Ruobing Dong, Lee Hartmann, and Takayuki Muto

ISIMA project report

ABSTRACT

Using Whitney's Monte Carlo radiative transfer code, we simulate the near IR scattered light images in both intensity and polarized intensity for a series of axisymmetric protoplanetary disk models. By measuring the properties of the images, we study the detectability of both the disks and the features of giant planet formation at early stage (i.e. gaps opened by the planets) in real observations, and the connection between the detected disk structure and the intrinsic properties of the system. We use real point spread functions of Subaru telescope to convolve the images, in order to synthesize realistic images with the smallest spatial resolution and inner working angle which ground based instruments can provide at present. In the models without gaps, the effects of the disk depletion factor, mass, and flareness on the images are investigated, while for the models with a gap, we focus on the dependence of the detectability of the gap on the gap position, width, and depletion factor. Qualitatively, the more massive and more flared the disk is, the brighter the disk is. The gap is only visible when the disk is visible, and the deeper and wider the gap is, the larger the contrast level of the gap is.

1. INTRODUCTION

Until recently, most exoplanets were discovered by radial velocity searches. However, the last few years saw booming development of alternative detection methods, in particular the direct imaging technique. Recently, 8-m class telescopes with adaptive optics (AO) and coronagraph technique have started not only detecting extrasolar planets but also revealing the complexity and diversity of protoplanetary disks around young stars, where planetary systems like our own can form. With adaptive optics, coronagraph, and advanced speckle removing techniques, current direct imaging observations can probe nearby protoplanetary disks to an inner working angle of $0.15''$ with a spatial resolution $\sim 0.06''$, and a great detail of the disk surface structure can be revealed (Hashimoto et al. 2011).

On the other hand, recent years also witnessed a great leap in the theoretical study of the protoplanetary disks. Two main planet formation mechanisms have been invented, namely the core accretion model and the gravitational instability model, while the applicable range and the details of each model remain uncertain. On the numerical simulation side, with the computational power provided by supercomputers, people are modeling the disks with ever great details and realistic physics. Specifically, the investigation of the effects of having planet(s) in protoplanetary disks, namely the gap opening phenomenon and the planetary migration, have drawn a lot of attention in the community.

However, while both the observational and theoretical sides of planetary disk study have advanced greatly, the link between the two is still underdeveloped at present. The morphological diversity of observed protoplanetary disks has not been well connected with their theoretical underlying origins, such as planets, magnetorotational instability (MRI), and gravitational instability (GI). Only in the last couple of years some very preliminary attempts have been made in this area (Hashimoto et al. 2011). Furthermore, some of the key questions in the observations, such as under realistic observational condition, what kind of features of giant planet formation can be detected with current instrument, have not been answered yet.

The goal of our ISIMA project is to fill this gap – to connect the observed protoplanetary disk structure/morphology with the theoretical disk/planet-formation models, and specifically, to uncover the signal of the unseen planets inside the disks via the perturbations of the disk morphology that they produce (i.e., gaps). To do so, we carry out radiative transfer modeling of protoplanetary disks using a Monte Carlo radiative transfer code (Whitney et al. 2003a,b) to synthesize disk images. To compare with the results from the ongoing direct disk imaging projects, we focus on the near infrared (NIR) wavelengths (namely the J, H, and K bands) for the moment. At these wavelengths the disk thermal emission is negligible beyond $\sim$ 1AU, and the observed disk light is the star light being scattered at the surface of the disk.

As present, several large ground based telescopes are currently carrying out plans to directly image protostellar disks in NIR wavelength. Among them, the 8-m Subaru telescope is the first one to commit a strategic class project – the Subaru Strategic Exploration of Exoplanets and Disks (SEEDS, Tamura 2009) using High-Contrast Coronographic Imager for Adaptive Optics (HiCIAO). Using 120 Subaru telescope nights in five years, the SEEDS project is searching for giant planets and directly imaging protoplanetary/debris disks mainly around $\sim$ 500 nearby solar-type or more massive young stars. The protoplanetary disk targets in the project are chosen from the young stellar objects in nearby star-forming regions, some being new targets with large infrared intrinsic polarization, while

the debris disk candidates include both well-known and newly discovered ones from the Spitzer and AKARI satellites. With excellent AO and coronagraph system, and speckle removing techniques, SEEDS have achieved high angular resolution ($\sim 0.06''$) and small inner working angle ($\sim 0.15''$) in direct disk imaging (Hashimoto et al. 2011). This survey will address some key issues in exoplanet/disk science, such as the evolution of protoplanetary and debris disks including their morphological diversity, and the link between exoplanets and circumstellar disks (Tamura 2009). Our project is oriented by the purpose of enabling comparisons between the synthesized images and real observed images from SEEDS, so that the instrument performence of SEEDS with HiCIAO is used in our modeling (see Section 2.2).

In the field of direct disk imaging, polarized intensity (PI=$\sqrt{Q^2 + U^2}$, where Q and U are two components in the Stokes vector) is often measured along with the full intensity (I in the Stokes vector), in order to achieve finer spatial resolution and smaller inner working angle. While the star light is usually nearly unpolarized, the scattered light from the disk is highly polarized ($> 30\%$) due to dust scattering property. In Polarimetric Differential Imaging (PDI) mode in SEEDS, the incoming light is split into beams with different polarizations, and then they are subtracted from one another. The speckles in direct disk observations are due to residual wavefront error and instrumental effects, so they are usually unpolarized and can be reduced by subtracting images acquired at different polarizations (Hinkley et al. 2009). While the subtraction procedure reduces the intensity of speckles, light scattered from disks is highly polarized and therefore survives the differencing process (Dressing 2010).

At last, we note that the techniques we developed and the results from our projects could also be used for other purposes. First, the radiative transfer modeling of the (polarized) scattered light in a circumstellar disk can also be used to model debris disks, and provide critical insight in understanding the results from ongoing direct debris disks imaging projects, such as SEEDS and Gemini Planet Imager (GPI, Macintosh et al. 2006). Second, it is also possible to include more wavelengths into our modeling (to do so the thermal emission of the dust needs to be considered) to model an entire spectrum of a protoplanetary disk, which could be compared with the observed spectral energy distribution (SED). Specifically, recent observations saw some disks with unusual flareness through SED, which we could investigate with the tools developed here.

The structure of the report is as following. In Section 2 we discuss the radiative transfer code which we use and the instrument response we employ in our modeling. In Section 3 we present the results we have so far. A short summary and a future plan is provided in Section 4.

2. Method

In this section, we introduce the code we use to do the disk radiative transfer modeling, and the instrument response we employ to synthesize the images.

2.1. The code and the method

We use the Monte Carlo radiative transfer code developed by Whitney et al. (2003a,b). Monte Carlo method is a commonly used method to study radiative transfer process in multi-dimensional geometries. In our case, we launch a certain number of photons from the central star, then the code simulates the transport of each individual photon (i.e., scattering, absorption, and emission) using probabilistic methods, while the photons experience 'random walks' in the disk. We model the entire disk with two components: A thick disk with normal ISM grains, and a thin disk with bigger grains. The two components have different masses, different dust properties, and different scale heights, but otherwise identical properties. The thick disk contains pristine dust grains in the star forming environment where the initial core collapse takes place, while the thin disk is meant to mimic the dust coagulation and settling effect. Observations show that protoplanetary disks disappear in $\sim$ 10Myr after their formation (Hartmann et al. 1998), which presumably is the result of coagulation and settling of the dust grains. The dust in the thin disk is at the middle stage of the dust evolution between initial ISM grains and final planetesimals. We adopt the dust model for both the thick and thin disk from Whitney et al. (2003a,b), and their properties are shown in Figure 1. The images that we show in this report are all in H band ($1.6\mu m$).

2.2. Realistic point spread function

The radiative transfer code produces a surface brightness map of the entire disk and star system, whose spatial resolution is only limited by the grid size of the system and the pixel size of the images. To obtain more *realistic* images which have the resolution of real observations and which can be directly compared with real observed images, the raw images have to be convolved by the point spread functions (PSFs) of the instrument. Specifically, the disk pixels in the flux map needs to be convolved by the PSF with no coronagraph, which is determined by the AO performance, and the star pixel (a single pixel at the center of the raw image) needs to be convolved by the PSF with the coronagraph, which is determined by both the AO performance and the coronagraph.

In our model, we use the real Subaru PSF in H band to convolve the images (SEEDS

instrument team, private communication), which are shown in Figure 2. The left panel shows the PSF without a coronagraph, which is obtained by taking an unsaturated image of the reference star HIP82265 with an integration time of 9.7 seconds. The FWHM of this PSF is $\sim 0.048''$, which is nearly a diffraction limited value for an 8-m telescope ($\sim 0.042''$). The integrated flux within a circle of $0.25''$, $0.5''$, and $1''$ from the star is 69%, 80%, and 88% of the total flux. We use this PSF to convolve each disk pixel which is not blocked by the coronagraph. The middle panel shows the full intensity PSF with a coronagraph for the (mask size $0.3''$ in radius) using the reference star HD166903 with an integration time of 30sec, while the right panel shows the polarized intensity PSF (5σ detection limit in the PDI mode) with a coronagraph (mask size $0.15''$ in radius) using the same reference star. We use these two PSFs to convolve the star pixel in I and PI images (the total disk flux which is blocked by the coronagraph is added to the star pixel). Note that to generate the PI images, we still convolve the star pixel in the I image and add this convolved star image to the convolved PI disk image.

The contrast ratio (defined to be the ratio of the intensity in the PSF images with a coronagraph to the peak intensity in the PSF image without a coronagraph) of the I and PI PSFs as a function of radius is shown in Figure 3. While the contrast ratio of the I PSF drops steadily when moving away from the center, for the PI PSF it appears to reach a finite asymptotic value beyond $\sim 1''$. This phenomenon is caused by the read-out noise. For the I image, its read-out noise oscillates around 0 with an average being 0, so the contrast ratio of the I image drops to 0 when moving away from the center. On the other hand, for the PI image, since PI=$\sqrt{Q^2 + U^2}$, the read-out noise will always be positive, and the PI PSF intensity gradually converges to this background finite read-out noise when moving away from the center. At the moment we are not sure what the instrument team does in post processing of real observational images, so we keeps the PI PSF as shown here. But in principle, the finite background read-out noise in the PI PSF could be removed.

3. Results

In this section, we present our results, which is a parameter space exploration of the radiative transfer modeling. All the models in the report are axisymmetric (so 2D models). To carry out the study, first we fix a fiducial disk model with no planets, then we measure the properties of the images generated from this model. Then, we vary one disk parameter at one time while keeping the others fixed, to study the effects of several parameters on the images. Last, we put a gap in the fiducial disk model, and we vary the properties of the gap to study their observable effects.

3.1. The fiducial model

For both the thick and the thin disk structure, we use a standard flared accretion protoplanetary disk model, whose density profile is shown in Equation (1) (Whitney et al. 2003a, Equation (3)):

$$\rho = \rho_0 \left[1 - \sqrt{\frac{R_\star}{\varpi}}\right] \left(\frac{R_\star}{\varpi}\right)^\alpha \exp\left\{-\frac{1}{2}\left[\frac{z}{h(\varpi)}\right]^2\right\} , \quad (1)$$

where ϖ is the radial coordinate in the disk midplane and the scale height increases with radius, $h = h_0 (\varpi/R_\star)^\beta$. For all the models here, we adopt $\beta = 1.25$ and $\alpha = 2.25$. For the thick disk, we set $h_0 = 0.01 R_\star$, giving a scale height at the radius 100AU of 10 AU. For the thin disk, we set $h_0 = 10^{-3} R_\star$. We define the disk depletion factor $\Delta_{\rm disk}$ to be

$$\Delta_{\rm disk} = \frac{M_{\rm thick}}{M_{\rm thick} + M_{\rm thin}} \quad (2)$$

where $M_{\rm thick}$ is the mass of the thick disk, $M_{\rm thin}$ is the mass of the thin disk, and $M_{\rm total} = M_{\rm thick} + M_{\rm thin}$ is the total mass of the disk.

For the central source, we use a 4350K star with a radius of $1.52 R_\odot$, and its SED is adopted from Robitaille et al. (2006). With a standard Shakura & Sunyaev accretion rate of $10^{-8} M_\odot$/yr, the total luminosity of the system is $0.92 L_\odot$. There is no outside illumination, no envelope, and no bipolar cavity in the system. For the fiducial model, we set $M_{\rm total} = 0.01 M_\odot$, and $\Delta_{\rm disk} = 1$ (so no depletion, or no thin disk component). The disk extends from an inner radius of 0.05 AU (the dust destruction radius) to an outer radius of 500 AU. There is no gaps, no spiral arms, and no warps in the fiducial disk model. For the output, we set the distance to the system to be 100 pc, so 1AU=0.01″ on the images. The FWHM of the PSF without a coronagraph which we use to convolve the disk is $\sim 0.05''$, which translates to ∼5 AU at this distance.The pixel size is 0.01″. The radius of the coronagraph is 0.3″ for the I images, and 0.15″ for the PI images.

The face-on I image (inclination angle $\theta = 0°$) of the fiducial system is shown in Figure 4. The left panel shows the raw image which is produced by the radiative transfer modeling. As we discussed in Section 2.2, the raw image needs to be convolved by the instrument PSF to get realistic images. The middle left panel shows the convolved disk image, which we produce by smearing out every pixel in the disk that is not blocked by the coronagraph by the Subaru HiCIAO PSF without a coronagraph (left panel in Figure 2). The middle right panel shows the convolved star image, which we produce by smearing out the star pixel (the central pixel in the left panel with the total intensity of the central part of the

disk which is blocked by the coronagraph) by the intensity PSF with a coronagraph (middle panel in Figure 2). The right panel shows the final image, with the convolved disk image and the convolved star image adding up together. To mimic the effect of the coronagraph, we artificially mask out the central part of the final image, as in real observations. Figure 5 shows the final I and PI images for the fiducial model at three viewing angles.

For the $\theta = 0°$ and $\theta = 45°$ cases, we measured the radial profile of the surface brightness of the images. For $\theta = 0°$ image, we bin the pixels into 50 radially equally spaced annuluses. We calculated the average flux in each annulus, and plot it as a function of radius in Figure 6. For the I image, the convolved star light dominates the surface brightness within $\sim 1.5''$, while for the PI image, the disk essentially dominates the entire image (except at the edge of the image where the disk flux drops due to some edge effect). This is an illustration of why PI images are better in studying the disk structure in direct imaging. For the $\theta = 45°$ viewing angle, we measure the radial profile in three different directions, indicated in the left panel in Figure 7, and the radial profiles of the surface brightness in these three directions are shown in the right panel in this figure. The radial profile for the convolved star image is plotted as well for reference. Technically, the radial profile for the convolved star in different directions would be slightly different due to Poisson noise, but we ignore this difference and only plot the average value for simplicity.

3.2. Disk models without gaps

In this section, we vary three parameters from the fiducial model to study their observable effects: the disk depletion factor $\Delta_{\rm disk}$, the total disk mass $M_{\rm total}$, and the scale height of the (thick) disk h_0. We change one parameter at one time while keeping the other two at their fiducial values. The radial profiles of both the I and PI images for these models at face-on viewing angle are shown in Figure 8 (for depletion factor), 9 (for total disk mass), and 10 (for scale height of the thick disk).

Figure 8 shows that for the I image, as $\Delta_{\rm disk}$ dropping from 1 (mimicking the process that more and more dust coagulates and settles to the disk midplane), the surface brightness profile of the disk shifts downward while maintaining its shape until 10^{-4}. After this $\Delta_{\rm disk}$ the trend is reversed that the profile increases with decreasing $\Delta_{\rm disk}$, and the inner part of the curve drops which makes the peak of the profile moves outward to $\sim 0.7''$. For the PI image, the same patten repeats though the change seems to be smoother (the $\Delta_{\rm disk} = 10^{-5}$ curve). The most possible explanation for this change is that the density in the thick disk drops to such a low value at $\Delta_{\rm disk} \sim 10^{-4}$ that the thick disk becomes optically thin (radially) at this point (i.e., the optical depth τ reaches unit at this $\Delta_{\rm disk}$ from the star to the surface of the

thin disk). Before this point, the star light is scattered at the surface of the thick disk (the $\tau = 1$ surface) by the normal ISM grains. After this point, the star light penetrates the thick disk to reach the surface of the thin disk and gets scattered by the bigger grains which mimic the coagulated and settled grains (Figure 1). The profile change is due to both the change in the grain scattering properties, and the change in the scattering geometry. Another thing to notice is that as $\Delta_{\rm disk}$ drops the disk becomes fainter and the star light dominates in larger area in both the I and PI images (the convolved star image almost does not change), due to the fact that the $\tau = 1$ surface becomes flatter and the disk receives less photons from the star. For our fiducial model, when $\Delta_{\rm disk}$ drops below 10^{-3}, the disk becomes essentially invisible in the final I images, and only visible at the inner part in the final PI images.

Figure 9 shows that for both the I and PI disk images, when the total disk mass drops (note in this case $\Delta_{\rm disk} = 1$, so no thin disk component) the disk becomes fainter while the surface brightness profile becomes slightly steeper. Again we note that the visibility of the disk strongly depends on the total disk mass. The smaller the total disk mass is, the fainter the disk is, so the disk component weights less in the final image giving the convolved star image almost doesn't change. And again this is because the scattering surface gets flatter for lower mass disk and the disk receives less stellar irradiation.

Figure 10 shows when the disk becomes flatter, besides the expected trend that the disk becomes fainter due to less stellar irradiation receipt, the change in the scattering surface and the scattering angle eventually alter the general shape of the disk surface brightness profile at the inner part. At $h_0 \geq 3 \times 10^{-3}$ (corresponds to $h \geq 3$AU at 100AU) the disk profile peaks at the edge of the coronagraph and decreases outward. But at $h_0 = 10^{-3}$ the peak of the profile moves to $\sim 0.7''$ for both the I and PI image and it increases outward inside this radius. This effect would be useful in real observations to infer the disk flareness based on its surface brightness profile.

Before we end this section, there are two sets of interesting comparisons which we can make by comparing models from different parameter groups. Top two panels in Figure 11 shows the comparison between the $\Delta_{\rm disk} = 0$ model in Figure 8, and the $h_0 = 10^{-3}$ model in Figure 10. The common point in this two models is that they both have only one disk component with $h_0 = 10^{-3}$. For the $\Delta_{\rm disk} = 0$ model this component is the big grain settled disk, while for the $h_0 = 10^{-3}$ model this component is the normal ISM grain disk. The two disk surface brightness profiles share similar shape, while the normal ISM grain disk has a slightly shallower profile. Bottom panels in this figure shows the comparisons between $\Delta_{\rm disk} = 0.1$ model and $M_{\rm total} = 0.01$ model, and $\Delta_{\rm disk} = 0.01$ model and $M_{\rm total} = 10^{-3}$ model. The common point between the two models in each set is that they have the same thick disk (normal ISM grains) component. If this thick disk component is optically thick

so that the $\tau = 1$ surface lies in this component and the star light is primary scattered by the normal ISM grains, we should expect the profiles for both the I and PI disk iamges to be similar for the two models in each set, which is indeed the case (comparing the solid and dashed lines with the same color). The small difference is due to their different thin disk (settled grains) components, which plays a minor role in the scattering process if the thick disk is optically thick.

3.3. Disk models with one gap

In this section we study models with one gap. We vary the scale height of the thick disk (there is no thin component), but all the other not gap related parameters are the same as in the fiducial model. To model a gap, we simply decrease the density in the gap by a certain constant factor, and we define the gap depletion factor $\Delta_{\rm gap}$ to be the ratio of the density at the gap to its original density (i.e., the density determined by Equation 1). The gap parameters we investigate here include the gap position, the gap width, and the gap depletion factor. Figure 12 to 14 show the surface brightness profile for both the convolved disk and the final I and PI images at $\theta = 0$, for models with one gap at 300-350 AU, 100-150 AU, and 120-130 AU, respectively.

In general, the gap has two effects on the disk image. The disk profile sees a dip at the gap position, and the disk surface brightness outside the gap enhances comparing with the no gap model. The depth of the dip is primarily determined by the gap depletion factor. For the two wide gap cases (300-350 AU gap and 100-150 AU gap), the dip for the $\Delta_{\rm gap} = 0$ models is about a factor of 10 in both the I and PI disk images (except that in the model with 300-350 AU gap and $h_0 = 0.01$, the gap is somewhat shallower), while the surface brightness at the bottom of the dip for the $\Delta_{\rm gap} = 0.3$ models is about 30% of the no gap cases. In another word, the depth of the dip roughly agrees with the depth of the gap. For the narrow gap models (120-130 AU gap), this scaling relation breaks and the depth of the dip in the disk image appears to be much shallower than the depth in the gap. This is because (1) a narrow gap is intrinsically harder to be seen in the scattered light images, and (2) the gap width (10 AU) here is comparable with the resolution of the image ($\sim$5 AU). We note that the position of the dip in the 300-350 AU gap model with $h_0 = 0.01$ is slightly more inside comparing with the position of the gap, but again this may be due to edge effect. The enhancement of the disk surface brightness outside the gap is correlated with the gap property: the deeper and the wider the gap is, the more prominent the enhancement is.

On the other hand, the visibility of the gap in the final I and PI images is largely influenced by the relative brightness of the star since the observable signal of the gap is

diluted in the final image due to the stellar contamination. For the 100-150 AU and 120-130 AU gap models, the dip is almost invisible (i.e., the contrast of the gap to its surrounding is too low) in the I image while it is clearly visible in the PI image, since the star light in the PI image is much weaker than in the I image at this radius. For the 300-350 AU gap models, the signal of the gap is weakened in both the I and PI final images due to severe stellar contamination in this radius range. Also, the detectability of the gap is affected by the detectability of the disk itself, since if the disk is invisible at the first place then there is no way for the gap to be detected. In our cases here, gaps in more flared disks are more visible than gaps in flatter disks. In general, in real observations, whether a gap could be seen in a scattered light disk image will be determined by both the relative brightness of the disk and the star (which is determined by both their intrinsic brightness and the instrument response), and the position, width, and depth of the gap.

4. Summary and future work

We synthesize NIR scattered light images in both intensity and polarized intensity for axisymmetric protoplanetary disk models using Whitney's Monte Carlo radiative transfer code. The goal of this project is to connect theoretical disk-planet models with real observations, and to address the issue that what kind of disk and features of giant planet formation are detectable. We use realistic PSFs from Subaru telescope to convolve the images to achieve realistic effects. For each disk model, we generated images in three viewing angle ($\theta = 0°, 45°, 85°$), and we measure the radial profile of the images. We first models a series of disks without gaps, to study the effects of disk mass, depletion factor, and flareness. Then we put one gap into the disk model, to study the effects of gap position, width, and depletion factor. We find that the detectability of the disk and the gap strongly depends on these parameters. Qualitatively, the more massive and more flared the disk is, the more detectable the disk is. The gap is only visible when the disk is visible, and the deeper and wider the gap is, the larger the contrast level of the gap is.

In the near future, we would like to finalize the project, quantify the result of the detestability of the disk and the gap, and establish the connection between the observed disk structure with its intrinsic properties. In addition, we would like to add realistic noise into the image, and to investigate its effect on the results. The final goal is to answer the question that when observing a realistic system using realistic instrument at present, what kind of feature of the giant planet formation is detectable. Also, using the same simulations and technique here, we can generate SEDs for the models, and we can compare them with real observations to infer the properties of the observed system, especially the flareness of

the systems. Eventually, we are planning to use disk profiles directly from (M)HD disk simulations, to study the effect of realistic gap profile, and various physics, such as MRI and GI.

Acknowledgments

We thank Eugene Chiang and Zhaohuan Zhu for useful discussion and comments. R.D. would also like to thank Pascale Garaud and the whole ISIMA organizing committee for such a wonderful and fantastic summer in Beijing. It's a great pleasure to be in ISIMA!

REFERENCES

Hashimoto, J., et al. 2011, ApJ, 729, L17

Dressing, C. D. Undergraduate thesis, Princeton University

Hartmann, L., Calvet, N., Gullbring, E., & D'Alessio, P. 1998, ApJ, 495, 385

Hinkley, S., et al. 2009, ApJ, 701, 804

Macintosh, B., et al. 2006, Proc. SPIE, 6272,

Robitaille, T. P., Whitney, B. A., Indebetouw, R., Wood, K., & Denzmore, P. 2006, ApJS, 167, 256

Tamura, M. 2009, American Institute of Physics Conference Series, 1158, 11

Whitney, B. A., Wood, K., Bjorkman, J. E., & Wolff, M. J. 2003, ApJ, 591, 1049

Whitney, B. A., Wood, K., Bjorkman, J. E., & Cohen, M. 2003, ApJ, 598, 1079

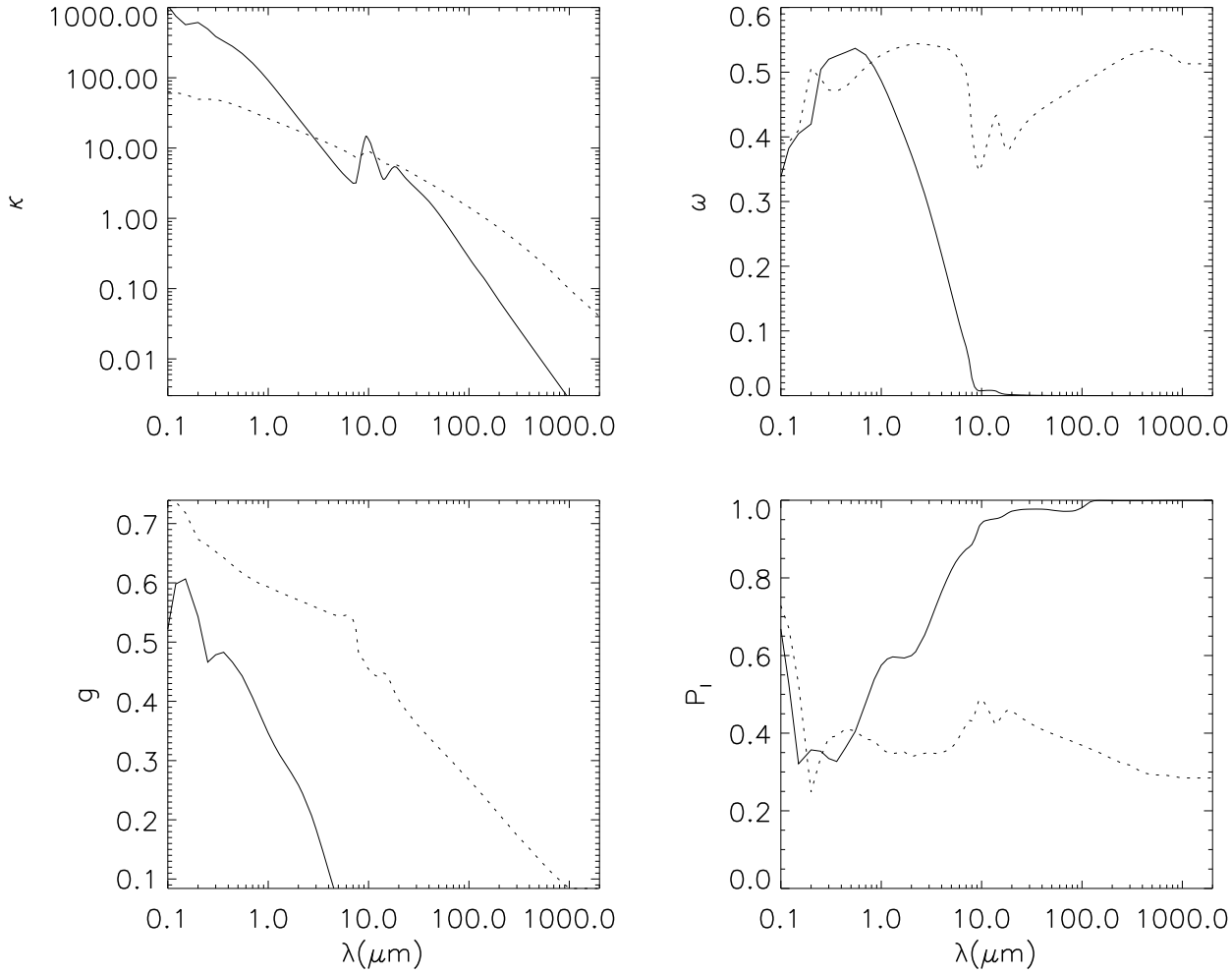

Fig. 1.— The dust properties for the two dust models we use in the modeling. The solid line is the dust in the thick disk, and the dashed line is the dust in the thin disk. The panels are (from top to bottom, left to right): Opacity κ, albedo ω, average cosine of scattering angle g, and maximum polarization P_l.

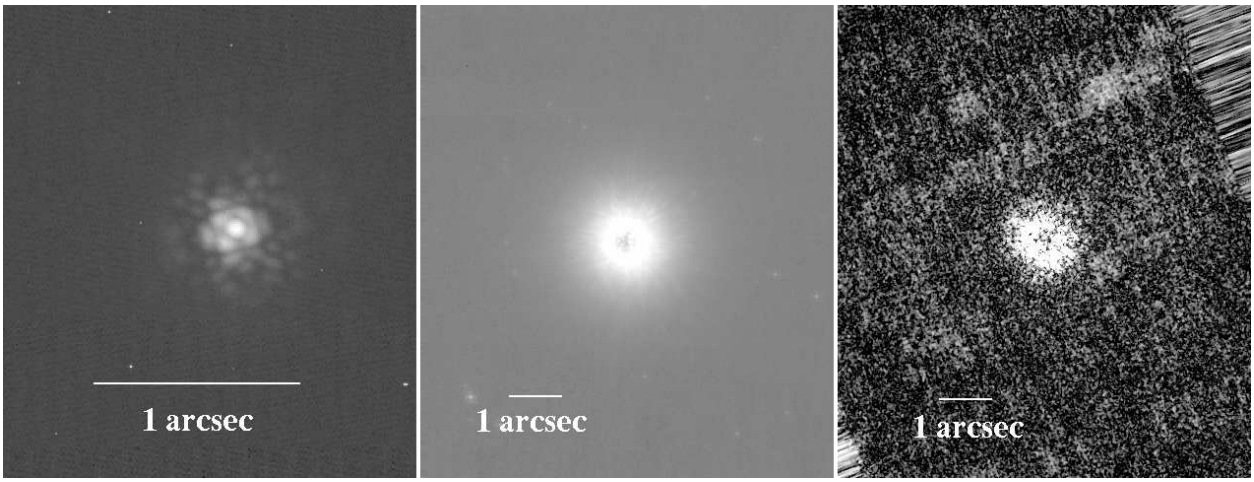

Fig. 2.— The PSF we use to convolve the images. From left to right: PSF without coronagraph, which is used to convolve the disk; full intensity PSF with coronagraph, which is used to convolve the star and the central part of the disk in full intensity images; and polarized intensity PSF with coronagraph, which is used to convolve the star and the central part of the disk in polarized intensity images.

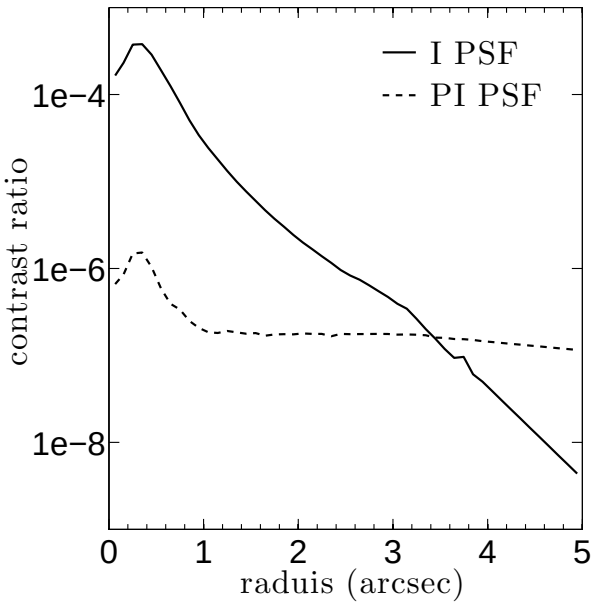

Fig. 3.— The contrast ratio as a function of radius for the I and PI PSF.

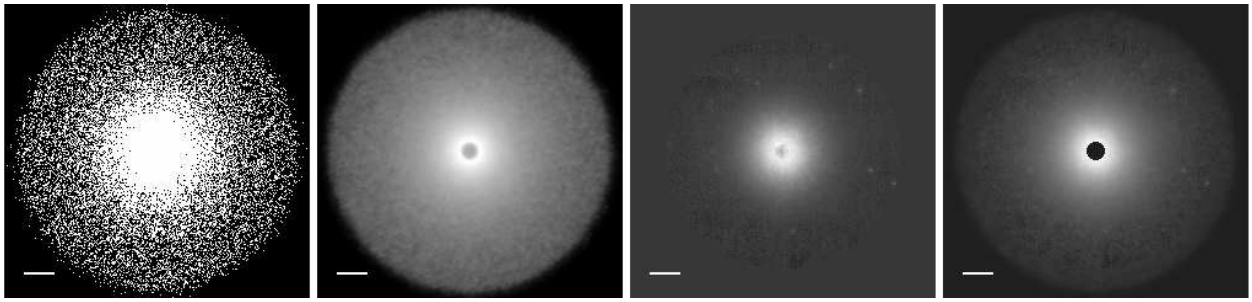

Fig. 4.— The face-on I images of the fiducial model. Left to right: the raw image, the convolved disk image, the convolved star image, and the final image. The horizontal bar in each panel indicates $1''$. The entire image size for every panel is $10'' \times 10''$.

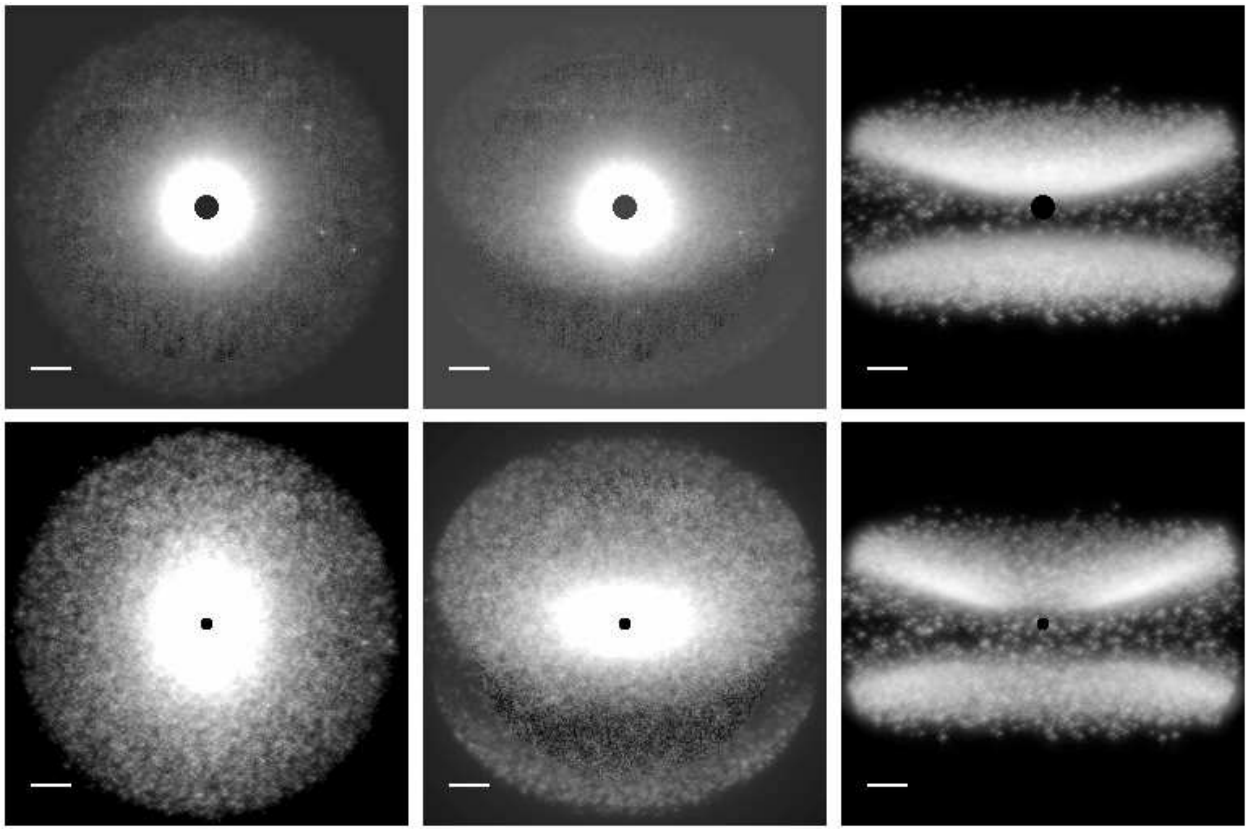

Fig. 5.— Images for the fiducial model. Top row: I images. Bottom row: PI images. Left column: face-on angle ($\theta = 0°$). Middle column: titled angle ($\theta = 45°$). Right column: edge-on angle ($\theta = 85°$). The horizontal bar in each panel indicates $1''$. The entire image size for every panel is $10'' \times 10''$.

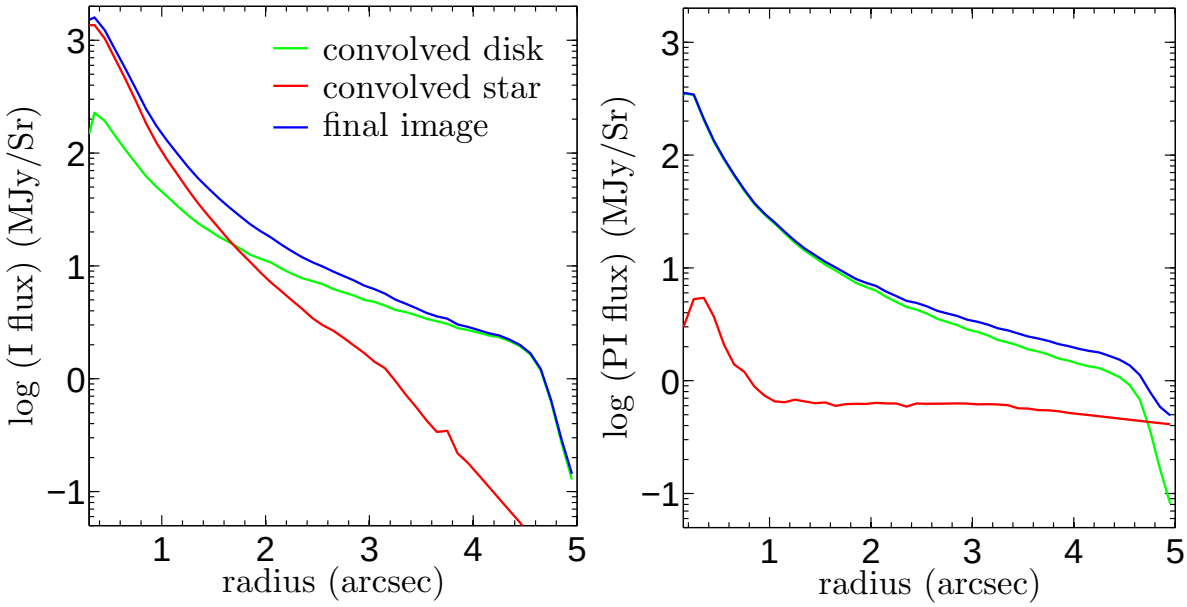

Fig. 6.— The surface brightness radial profile for the I and PI images of the fiducial model at face-on viewing angle.

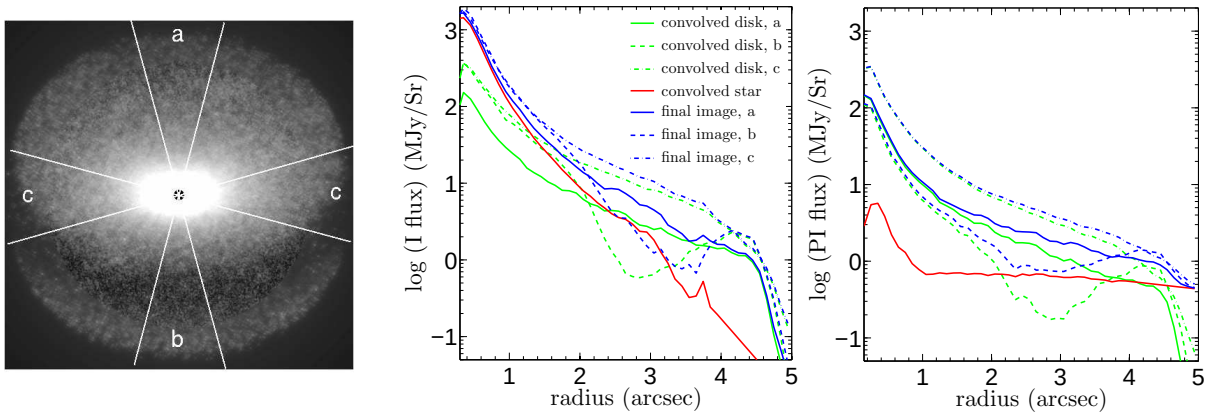

Fig. 7.— The radial profile for the I and PI images of the fiducial model at titled viewing angle ($\theta = 45°$). Left panel illustrates where the regions a, b, and c are.

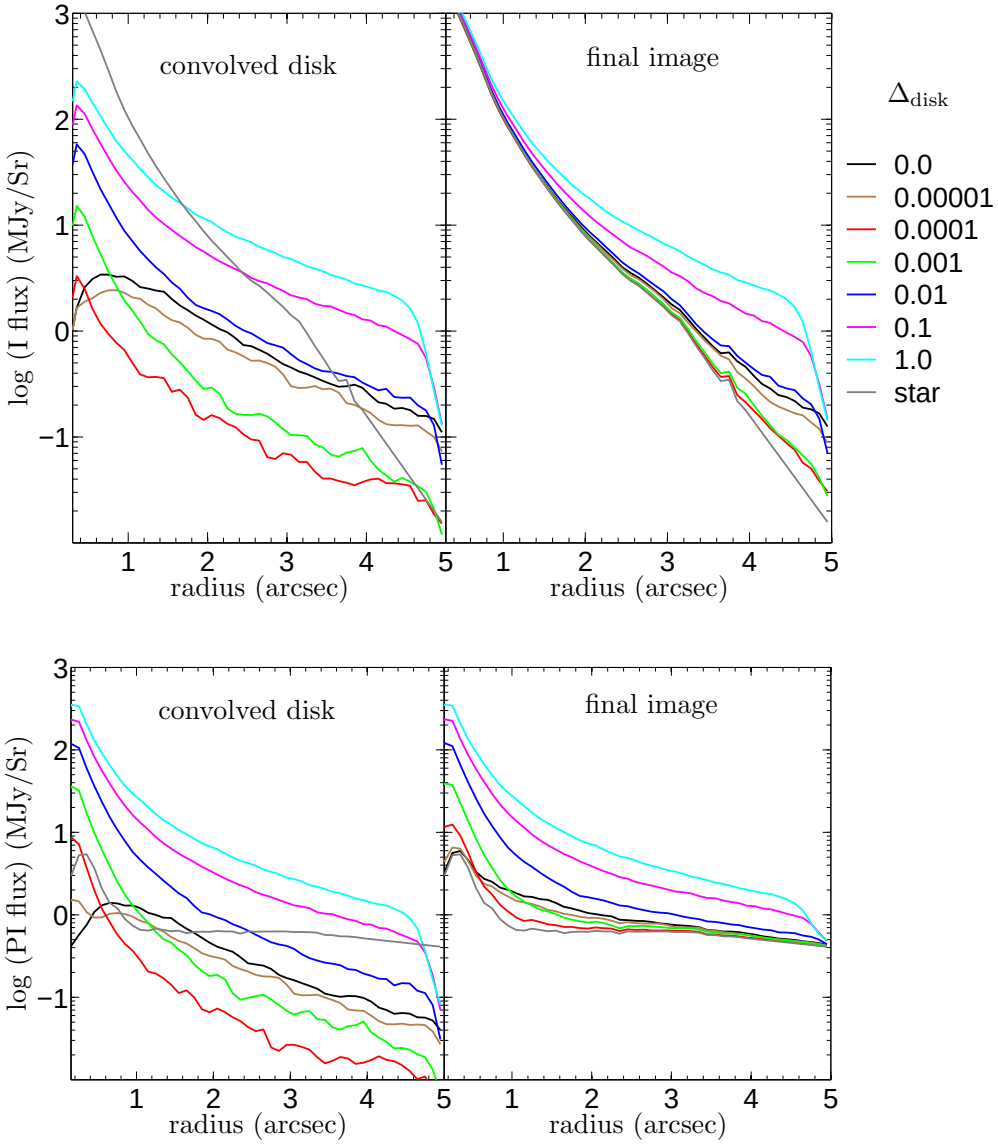

Fig. 8.— The radial profile of the I (top panels) and PI (bottom panels) images at $\theta = 0°$ for models with different depletion factor $\Delta_{\rm disk}$. The left panel in each set is for the convolved disk images, and the right panel in each set is for the final images. The radial profile of the convolved star image of the fiducial model is shown for reference (strictly speaking the convolved star image is slightly different for different models, but the difference is negligible.).

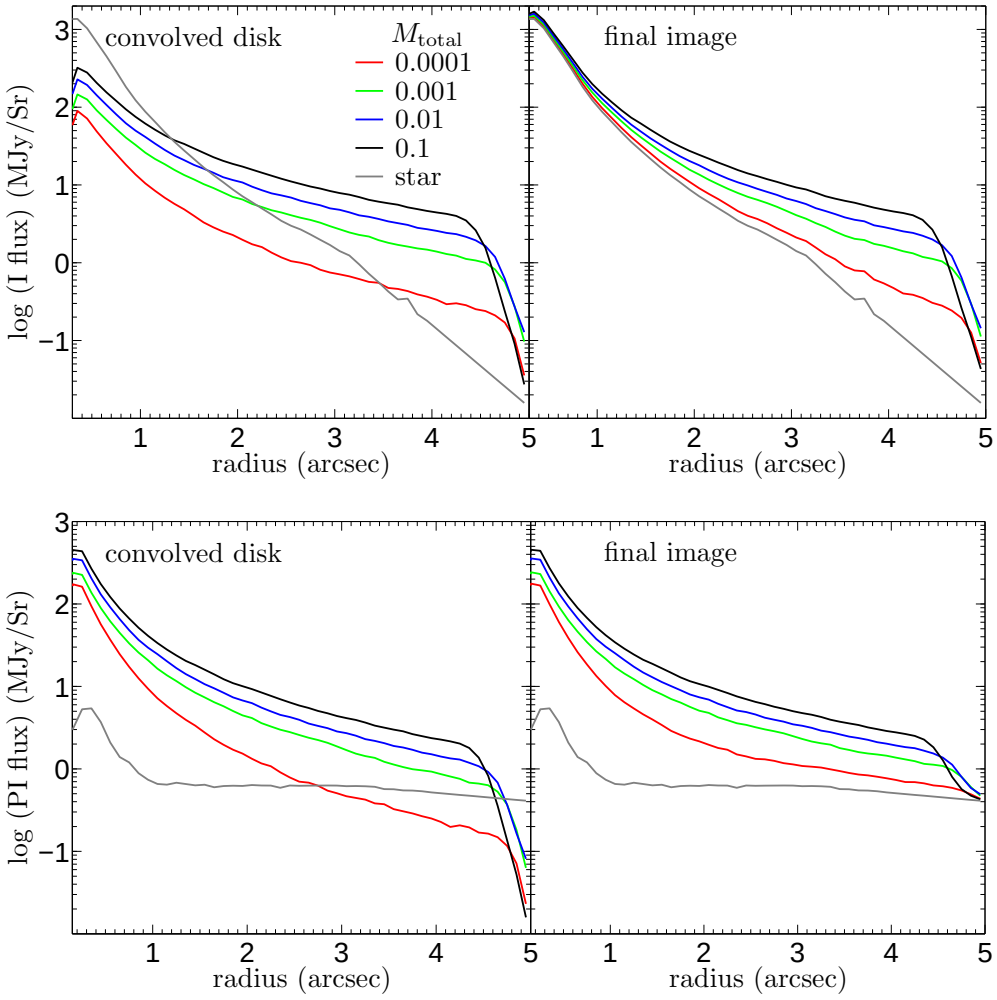

Fig. 9.— The same as Figure 8, but for models with different total mass $M_{\rm total}$.

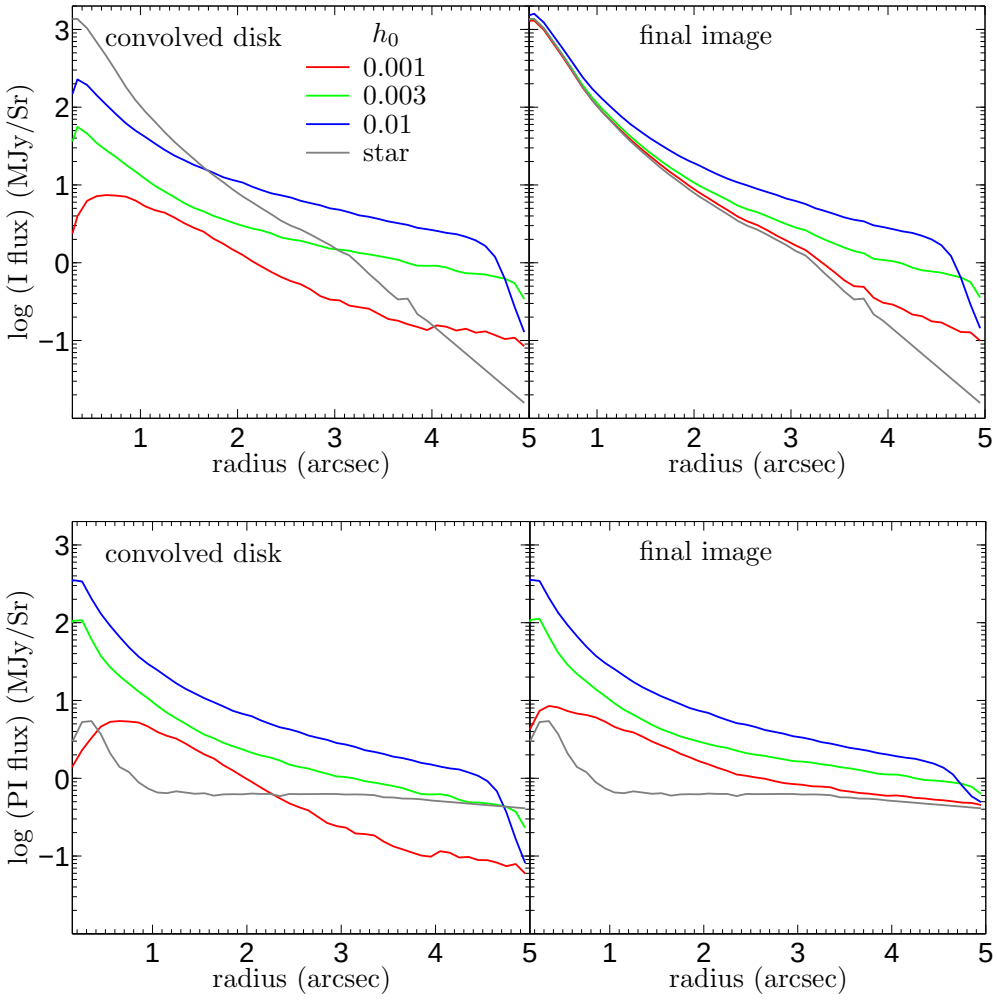

Fig. 10.— The same as Figure 8, but for models with different thick disk scale height h_0.

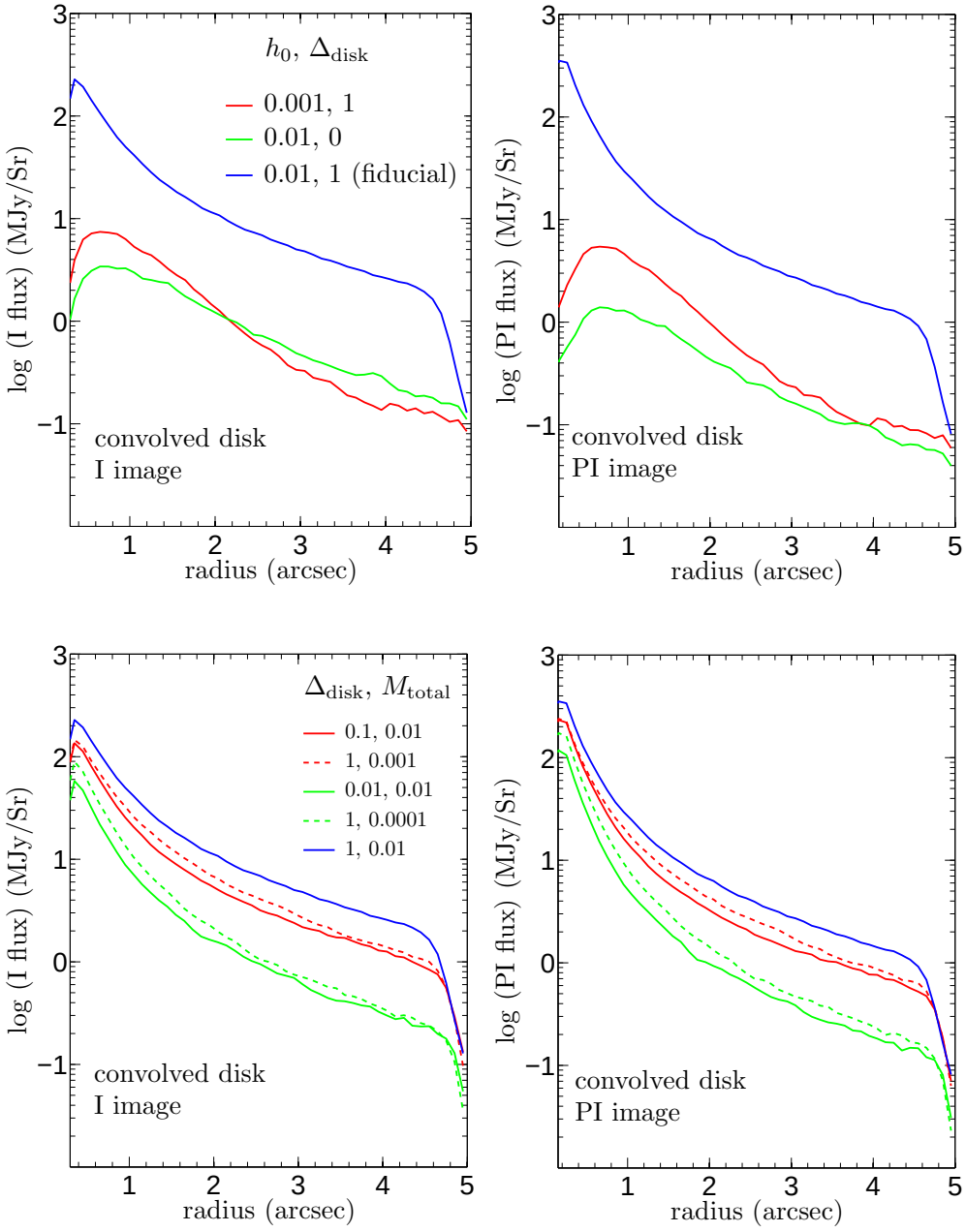

Fig. 11.— The radial profile for the I (left column) and PI (right right column) images for the $h_0 - \Delta_{\rm disk}$ comparison set (top row), and for the $\Delta_{\rm disk} - M_{\rm total}$ comparison set (bottom row).

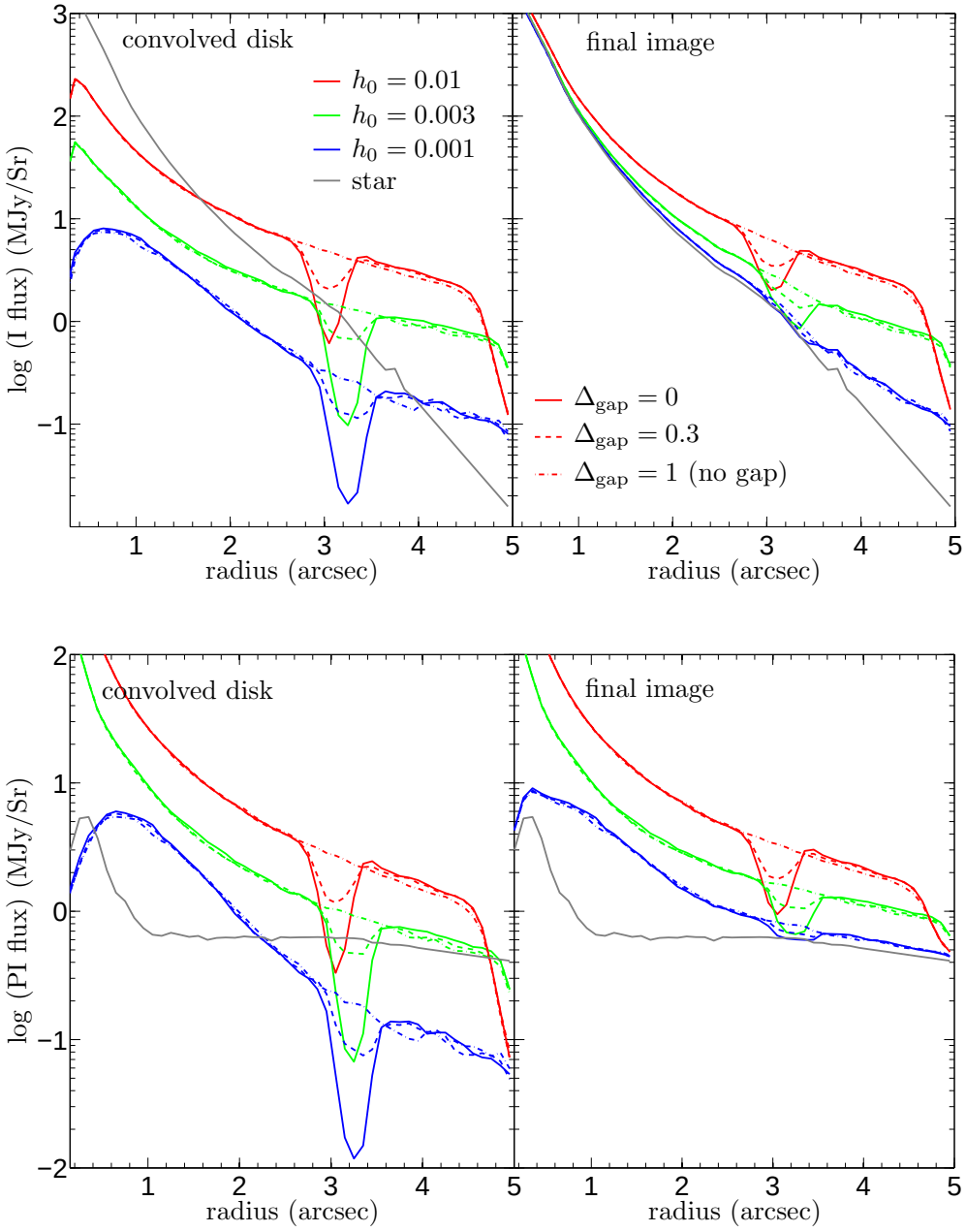

Fig. 12.— The radial profile for the I (top panels) and PI (bottom panels) images at $\theta = 0°$ of models with a gap at 300-50 AU. The left panel in each row is for the convolved disk images, and the right panel in each row is for the final images. In each panel, top set of three red lines are for models with $h_0 = 0.01$ (the same as the fiducial model), middle set of three green lines are for models with $h_0 = 3 \times 10^{-3}$, and bottom set of three blue lines are for models with $h_0 = 10^{-3}$. In each set of lines, the solid line is for $\Delta_{\rm gap} = 0$, the dashed line if for $\Delta_{\rm gap} = 0.3$, and the dash-dotted line is for $\Delta_{\rm gap} = 1.0$ (so no gap) model.

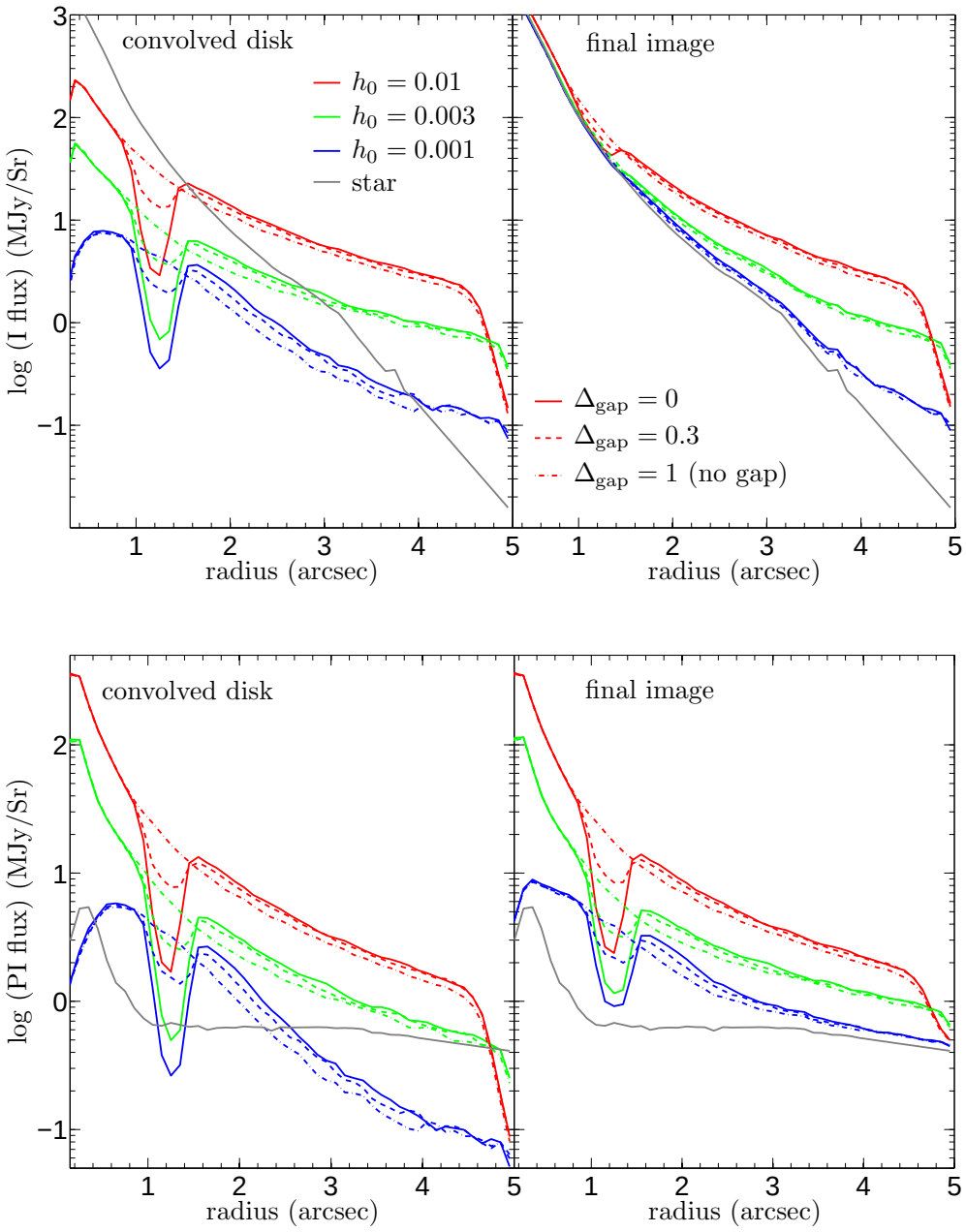

Fig. 13.— The same as Figure 12, but for models with a gap at 100-150 AU.

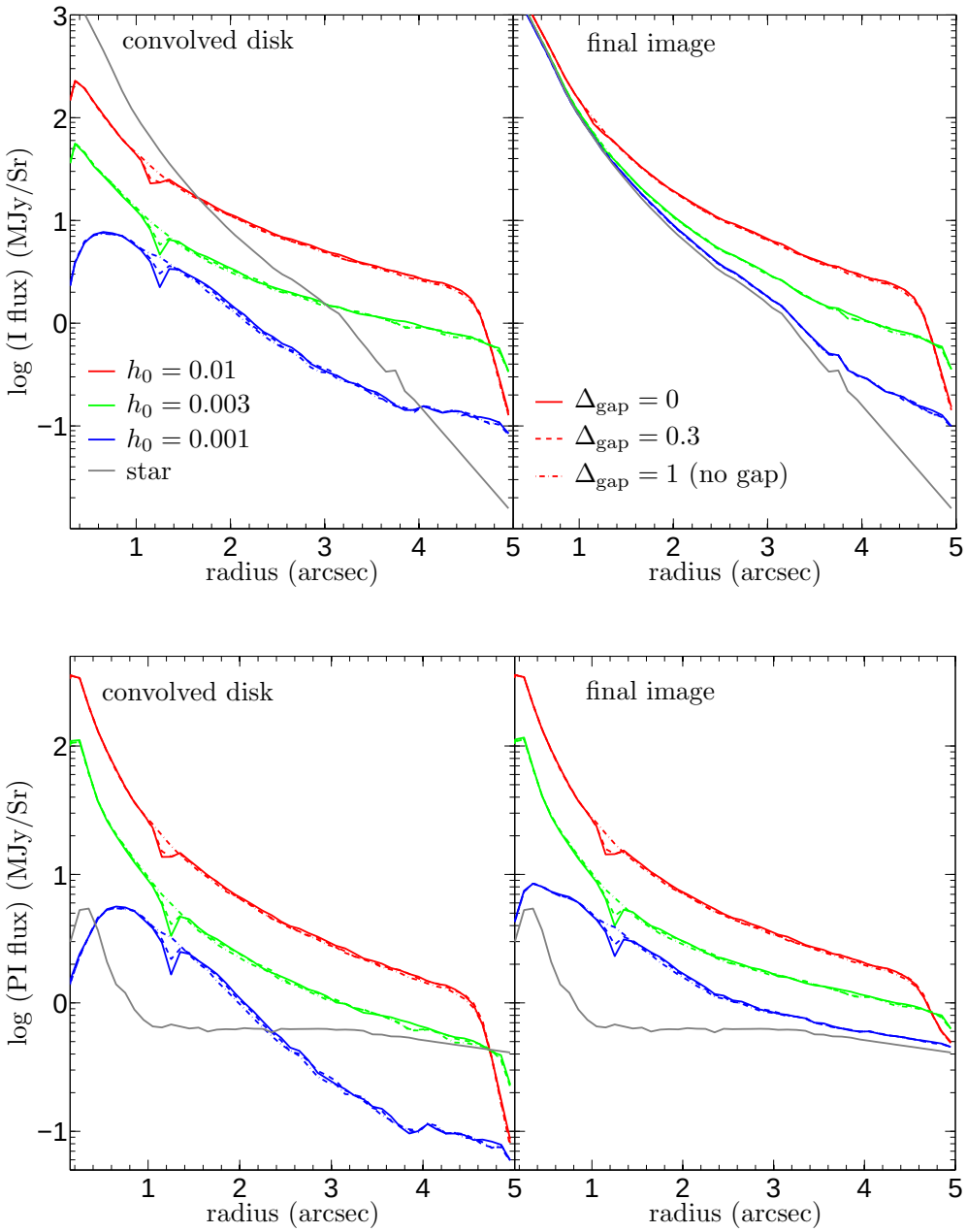

Fig. 14.— The same as Figure 12, but for models with a gap at 120-130 AU.